

Self-Calibrating Gaussian Splatting for Large Field of View Reconstruction

Youming Deng¹

Wenqi Xian²

Guandao Yang³

Leonidas Guibas³

Gordon Wetzstein³

Steve Marschner¹

Paul Debevec²

¹Cornell University

²Netflix Eycline Studios

³Stanford University

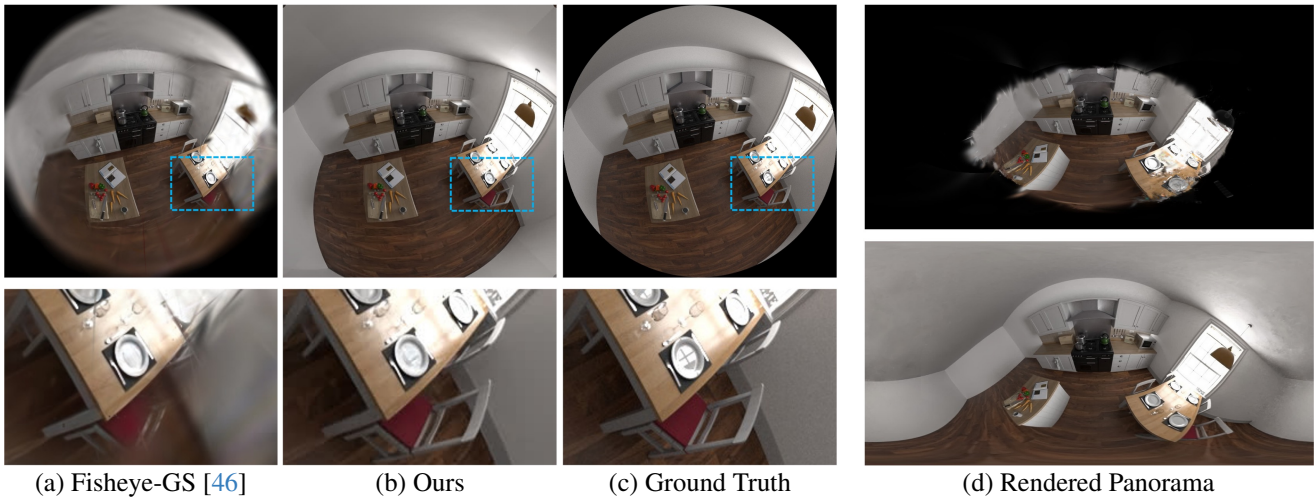


Figure 1. We introduce Self-Calibrating Gaussian Splatting, a differentiable rasterization pipeline with a hybrid lens distortion field that can produce high-quality view-synthesis results from uncalibrated wide-angle photographs. (a) Existing methods like Fisheye-GS [46] fail to accurately handle complex lens distortions due to the fixed traditional parametric distortion model. (b) Our method accurately models large distortions, especially in the peripheral regions, utilizing the entirety of highly distorted raw images for reconstruction. (d) Our method (bottom) provides extensive coverage, whereas conventional pipelines (top) can only recover the center.

Abstract

In this paper, we present a self-calibrating framework that jointly optimizes camera parameters, lens distortion and 3D Gaussian representations, enabling accurate and efficient scene reconstruction. In particular, our technique enables high-quality scene reconstruction from Large field-of-view (FOV) imagery taken with wide-angle lenses, allowing the scene to be modeled from a smaller number of images. Our approach introduces a novel method for modeling complex lens distortions using a hybrid network that combines invertible residual networks with explicit grids. This design effectively regularizes the optimization process, achieving greater accuracy than conventional camera models. Additionally, we propose a cubemap-based resampling strategy to support large FOV images without sacrificing resolution or introducing distortion artifacts. Our method is compatible with the fast rasterization of Gaussian Splat-

ting, adaptable to a wide variety of camera lens distortion, and demonstrates state-of-the-art performance on both synthetic and real-world datasets. More details and videos can be found at the project page: <https://denghilbert.github.io/self-cali/>.

1. Introduction

Recent advances in 3D scene reconstruction, such as Neural Radiance Fields (NeRFs) [48] and Gaussian Splatting (3DGS) [37], have shown remarkable success for high quality novel-view synthesis (NVS). However, these methods typically require dense image captures, relatively narrow FOV, and precise camera pose estimation from structure-from-motion (SfM) techniques [58, 59]. In practical applications, large FOV lenses such as fisheye lenses are often used in fields like robotics and virtual reality [18, 40] because they capture larger regions of a scene with fewer

images, enabling faster data collection and reconstruction. Yet, these lenses introduce significant geometric distortion, making accurate camera calibration and scene reconstruction challenging.

Sometimes, the intrinsic properties of wide-angle imaging systems can be pre-calibrated using specialized setups such as a room covered in calibration markers. But these processes can be slow and cumbersome. Polynomial camera distortion models, such as those implemented in OpenCV [10, 58], work well for standard lenses but struggle to modeling the complex and non-linear distortions of fisheye optics. As a result, many frameworks require fisheye images to be “undistorted” into perspective images before reconstruction, resulting in images with significant stretching and/or cropping relative as seen in Fig. 2.

To address these challenges, we explore self-calibration techniques that jointly optimize camera parameters with 3D scene representations. Such approaches have roots in methods that calibrate cameras without explicit calibration targets [15, 16, 53, 67]. More recently, self-calibration has been integrated into radiance fields and 3D Gaussian frameworks [34, 46, 49], where the photometric loss is used to refine both extrinsic and intrinsic parameters. However, these methods still lack the ability to accurately model the complex lens distortions typical for wide FOV imagery. This results in significant misalignment artifacts, especially in the peripheral regions.

In this work, we introduce Self-Calibrating 3D Gaussian Splatting, a differentiable rasterization pipeline that optimizes both camera lens distortion and scene representations using 3D Gaussians. Our approach is designed to be expressive enough to model diverse distortions while remaining computationally efficient and well regularized for stable training. Previous methods have attempted to handle lens distortion using grid-based ray offsets [34] or invertible neural networks [62]. While grid-based models are fast, they often produce noisy and unstable results when supervised solely by photometric loss. In contrast, neural network-based approaches offer better regularization but are prohibitively expensive when applied to each individual Gaussian.

To overcome these limitations, we propose a novel hybrid neural field that combines the strengths of both methods, striking a balance between expressiveness and computational efficiency, as shown in Fig 3. Specifically, our method adopts invertible Residual Networks [8] to predict displacement on a normalized sparse grid, followed by bilinear interpolation to generate a continuous distortion field.

For images with large fields of view, using a naive single planar projection results in severe pixel stretching and distortion, particularly in the peripheral regions. To mitigate this, we introduce a novel resampling strategy based on a cubemap representation, which evenly distributes im-

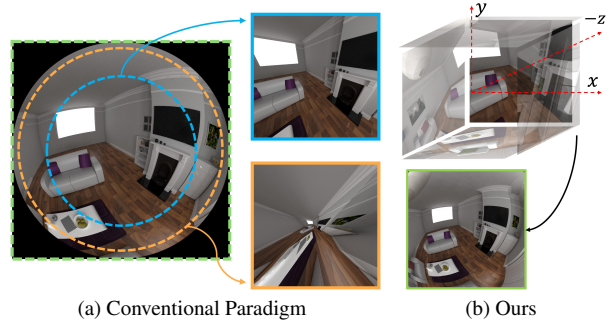


Figure 2. **Conventional Paradigm vs. Our Method.** (a) Conventional approaches require undistorting the image into perspective views compatible with 3DGS rasterization. As the field of view increases, pixel stretching becomes progressively severe, significantly compromising the quality of the reconstruction. (b) In contrast, our cubemap resampling strategy maintains a consistent pixel density across the entire field of view. This approach, combined with our hybrid distortion field, makes use of the peripheral regions (the annular area outside the blue box) without severe distortion or pixel stretching. Moreover, our method can handle fields of view all the way up to 180°, as demonstrated by the green box, allowing for comprehensive and accurate reconstructions.

age data across cubemap faces. This approach significantly reduces distortion artifacts and provides a clear, relatively undistorted omnidirectional view of the scene, preserving pixel resolution even in the outer areas.

To validate the efficacy of our method, we conduct extensive experiments on both synthetic datasets and several real-world scenes, including the FisheyeNeRF datasets [34] and our synectics Mitsuba dataset. Our system effectively calibrates camera parameters and lens distortion, achieving superior Gaussian Splatting performance compared to existing methods when using uncalibrated fisheye cameras. Importantly, our parametrization is not limited to a single fisheye camera model; rather, it is designed to be flexible and adaptable, accommodating a wide variety of camera models and real-world distortions seamlessly, all without the need for pre-calibration. This flexibility enables our method to fully leverage the unique capabilities of each available lens, enabling rapid scene capture with comprehensive coverage.

2. Related Work

Camera Modeling and Lens Distortion. Lens distortion is an inherent property of all cameras. In general, non-linear distortion can be formulated as:

$$\mathbf{x}_d = \mathbf{K} \cdot D(\pi(\mathbf{R} \cdot \mathbf{X} + \mathbf{t})), \quad (1)$$

where \mathbf{K} and $[\mathbf{R}|\mathbf{t}]$ are the intrinsic and extrinsic, respectively. $\pi(\cdot)$ denotes the pinhole projection, including dehomogenization to obtain 2D points \mathbf{x}_n on the image plane.

The distortion model $D(r(\mathbf{x}_n))$ is parameterized as a polynomial function of the radial distance:

$$D(r(\mathbf{x}_n)) = 1 + k_1 r^2 + k_2 r^4 + k_3 r^6 + \dots \quad (2)$$

where k_1, k_2, k_3, \dots are the parameters of the Brown-Conrady model [11, 17], derived from calibration, and $r = \sqrt{x_n^2 + y_n^2}$. Scaramuzza *et al.* [57] first proposed a unified model for larger FOV fisheye lenses, which has been adopted in several works [12, 42]. The most widely used fisheye model [32] describes the distortion as a function of the angular distance from the projection center:

$$D(r(\mathbf{x}_n)) = \frac{\theta}{r} (1 + k_1 \theta^2 + k_2 \theta^4 + k_3 \theta^6 + \dots), \quad (3)$$

where $\theta = \arctan(\frac{r}{1})$, and the distances of projected points to the image plane are normalized to 1. The 3D Gaussian [37] assumes a standard perfect pinhole camera model and typically requires COLMAP [58] to undistort images before reconstruction. To relax this constraint, recent methods [46, 49] adopt parametric models like Eq. (3) to extend 3D Gaussian Splatting techniques to fisheye images. However, these methods still rely heavily on camera calibration for accurate estimation and fix the projection in rasterization, making it difficult to generalize to various types of cameras. Works like [49] introduce ray tracing into the rasterization pipeline and approximate Gaussians bounding with icosahedron which potentially jeopardize the efficiency of rasterization. Some works [4, 45] also explore reconstruction from omnidirectional 360 panoramas, but the major difference is that panoramas require calibration to stitch two fisheye images and do not preserve raw geometric consistency at the stitching boundary. We address the aforementioned limitations by applying a hybrid distortion field that is compatible with the 3D Gaussian Splatting pipeline. Our experiments demonstrate existing methods such as Fisheye-GS [46] and ADOP [55] adopt traditional camera distortion models, such as those in Eqs. (2) and (3) into the rasterization process, are not expressive enough to handle the distortions present in large FOV cameras.

Self-Calibrating Reconstruction. The bundle adjustment process can be extended to include optimization of camera lens parameters as well as the poses. This way cameras do not need to be calibrated in a separate operation; this process is known as self-calibration [19, 30, 54, 68]. Camera calibration without a known calibration target is challenging as it relies on strong assumptions about the scene structures and geometric priors for establishing reliable 3D-2D correspondence [2, 6, 14]. Camera auto-calibration methods [19, 54, 68] extend this idea to derive camera intrinsics from multi-view observations of unstructured scenes, which was further advanced in recent studies [21, 22, 28]. Typically, the camera calibration process

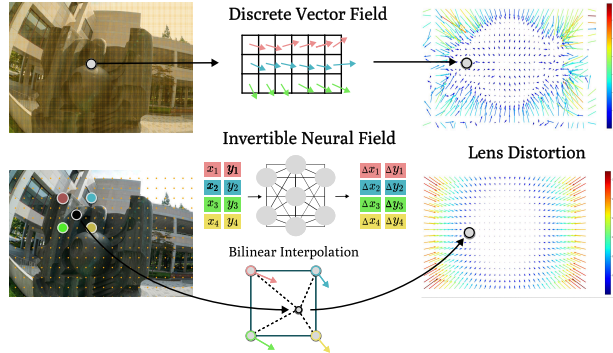


Figure 3. Overview of our method. In contrast to the explicit distortion vector field illustrated in the upper row, our hybrid approach maintains computational efficiency by leveraging explicit control points. Additionally, the regularization provided by the invertible neural field effectively balances the trade-off between the expressiveness and smoothness of the distortion field.

involves careful selection of appropriate camera lens models from a large family of high-order polynomial models and camera projection functions [20, 23, 36, 56, 60]. On the other hand, non-parametric models have been developed for broad applicability across different camera and lens combinations [13, 25, 29, 44], while additional regularization was needed to ensure the underlying distortion to be smooth [51]. With advances in differentiable rendering and rasterization pipelines [41, 65], recent works [34, 55, 62] showed that camera lens distortion can be optimized together with other parameters through a differentiable projection module. Prior works also adapt NeRF for panoramic inputs and fisheye distortions [27, 31, 43, 63]. These solutions usually use parametric models tailored for specific lenses of interest and are not generalizable to a wide variety of lenses types. SCNeRF [34] proposes to model a residual projection matrix and residual raxel parameters [26], which are interpolated on a sub-sampled pixel grid. Cam-P [52] proposes a novel preconditioner for the pose optimization, further improving the modeling of camera extrinsics and intrinsics jointly with NeRF. NeuroLens [62] optimizes lens parameters through an invertible neural network. This work builds on the insight of prior self-calibration methods and introduces a novel and efficient way of modeling lens distortion integrated with Gaussian Splatting.

3. Method

Given uncalibrated wide-angle captures, we aim to develop an algorithm that produces high-quality reconstructions using 3D Gaussians. Our method is designed to be robust to severe distortion in peripheral regions of images and various wide-angle lens effects. We achieve this through two key steps. First, we extend Gaussian splatting to support a broader range of camera models, such as fisheye lenses, as

discussed in Sec. 3.2. To model lens distortion, we apply a hybrid distortion field to diverse real-world scenarios where cameras with various distortions are used. Second, we replace the traditional single planar projection in 3DGS with cubemaps and introduce the depth sorting strategy accordingly, as detailed in Sec. 3.3.

3.1. Background of Gaussian Splatting

3DGS explicitly represents a 3D scene with a collection of Gaussians, each parameterized by a center $\mu \in \mathbb{R}^3$, a scaling vector $s \in \mathbb{R}^3$, and a quaternion $q \in \mathbb{R}^4$ representing the orientation. Each Gaussian G can be formulated as:

$$G(x) = e^{-(x-\mu)^T \Sigma^{-1} (x-\mu)}, \text{ where } \Sigma = R_q S S^T R_q^T, \quad (4)$$

where $S = \text{diag}(s) \in \mathbb{R}^{3 \times 3}$ is a diagonal matrix with the vector s on the diagonal, and $R_q \in \mathbb{R}^{3 \times 3}$ is the rotation matrix for the quaternion q . Each Gaussian is also associated with a d_c -dimensional vector c that stores spherical harmonic coefficients to represent the color of the Gaussian.

To produce an image from this set of Gaussians, we need to assume a projection function $\mathcal{P} : \mathbb{R}^3 \rightarrow \mathbb{R}^2$ that takes a 3D point $\mathbf{X} \in \mathbb{R}^3$ and projects it to pixel coordinates $\mathcal{P}(\mathbf{X}, \Theta) \in \mathbb{R}^2$ conditioned on camera parameters Θ . Under this projection function, the 3D Gaussians are projected to 2D for rasterization [69]:

$$\mu^{2D} = \mathcal{P}(\mu, \Theta), \quad \Sigma^{2D} = J_{\mathcal{P}}^T \Sigma J_{\mathcal{P}} \quad (5)$$

where $J_{\mathcal{P}} \in \mathbb{R}^{3 \times 2}$ is the affine approximation of the projection \mathcal{P} at point μ while parameterized by Θ . In the original 3DGS paper, the authors assume perspective pinhole camera models free of lens distortion. The final image for a set of Gaussians $G = \{(\mu_i, s_i, q_i, c_i)\}_i$ is produced using alpha blending [41, 65]. Specifically, the RGB color for pixel location u is given by the following equation:

$$\hat{I}(u) = \sum_{i=1}^{|G|} C_i w_i, \text{ where } w_i = \alpha_i \prod_{j \in \mathcal{N}_{< i}(G)} (1 - \alpha_j), \quad (6)$$

where $\mathcal{N}(G)$ is an ordered set of indices for relevant Gaussians to pixel location u sorted by depth, $\mathcal{N}_{< k}$ indicates the first $k - 1$ element of \mathcal{N} , $C_i \in \mathbb{R}^3$ is the view-dependent RGB color, α_i is the opacity given by applying Eq. 5 on the 2D Gaussians. Finally, this set of 3DGS is optimized using a photometric loss:

$$\mathcal{L} = (1 - \lambda) \mathcal{L}_{\ell_1}(I, \hat{I}) + \lambda \mathcal{L}_{D-SSIM}(I, \hat{I}), \quad (7)$$

where λ is the loss weight, \mathcal{L}_{ℓ_1} is the L1 loss and \mathcal{L}_{D-SSIM} is the D-SSIM [5] loss. The parameters of Gaussians G are usually optimized using gradient-based algorithms together with adaptive control. [37].

3.2. Lens Distortion Modeling

In this section, we extend the Gaussian splatting technique to accommodate a broader class of camera lenses, including fisheye and wide-angle cameras by modeling the lens distortion. Lens distortion is typically captured by a distortion function defined in camera coordinates. A Distortion function $\mathcal{D}_{\theta} : \mathbb{R}^2 \rightarrow \mathbb{R}^2$ parameterized by θ maps pixel locations from a rectified image to locations of a distorted image. Ideally, the mapping \mathcal{D}_{θ} should be: 1) expressive enough to model various lens distortions, 2) well regularized such that it can be optimized together with the 3D scenes, and 3) efficient so that it does not add significant overhead. While existing methods have explored using parametric camera models, grid-based methods, and deep-learning methods, none of these methods perfectly satisfy all three criteria.

Grid-based method. The simplest way to implement a generic camera model is to explicitly optimize for the distortion in a grid of pixel coordinates and apply bilinear interpolation to extract a continuous distortion field:

$$\mathcal{D}_{\theta}(\mathbf{x}) = \mathbf{x} + \text{interp}(\mathbf{x}, \theta), \quad (8)$$

where the optimizable parameters $\theta \in \mathbb{R}^{H \times W \times 2}$ are a $H \times W$ grid storing 2D vectors representing the distortion. Bilinear interpolation function $\text{interp}(x, \theta) = W(x, \theta) \cdot \theta$, with $W(x, \theta) \in \mathbb{R}^{H \times W}$ being the bilinear interpolation weights of location x . Such a grid-based method is expressive and efficient, since $W(x, \theta)$ is sparse (*i.e.*, weights are zeros except for the those in the neighbor nodes of x) and one can increase the grid resolution to model more complex functions. The grid-based method, however, lacks the proper smoothness needed to model lens distortion, resulting in overfitting and suboptimal solutions (Fig. 3 Top).

Invertible Residual Networks. An alternative way to model the distortion is using a neural network with appropriate inductive bias. NeuroLens [62] proposes to use invertible residual networks [8] to represent non-linear lens distortions as a diffeomorphism. Specifically, the deformation mapping is modeled by a residual network:

$$\mathcal{D}_{\theta}(x) = F_L \circ \dots \circ F_1(x), \quad F_i(z) = z + f_{\theta_i}^{(i)}(z), \quad (9)$$

where $f^{(i)}$ is a neural network parameterized by θ_i with Lipschitz constant bounded by 1 (*i.e.*, $|f_{\theta}^{(i)}(x) - f_{\theta}^{(i)}(y)| < |x - y|$ for all x, y , and θ). $f_{\theta_i}^{(i)}$ represents a residual block with 4 linear layers. L denotes the number of blocks, which is 5 in our case, and the circle denotes function composition. Such constraints make the network invertible, and its inverse can be obtained using a fixed-point algorithm [8].

While an invertible ResNet provides both expressivity (*i.e.*, being able to fit many lenses) and regularity, it is computationally expensive to deploy it directly to 3DGS for several reasons. To compute the alpha-blending weights α_i and w_i when rendering an image in Eq. (6), forward and backward passes of \mathcal{D}_θ for each Gaussian are required. This is computationally expensive for large-scale scenes with millions of 3D Gaussians, and motivates us to find a more efficient solution that can leverage the inherent inductive bias of the invertible ResNet. We show more ablation comparisons in the supplementary to demonstrate the effective regularization of iResNet compared with regular ResNet.

Hybrid Distortion Field. Given that the grid-based method is efficient yet tends to overfit, while the invertible ResNet has an appropriate inductive bias but is not efficient, we propose a hybrid method that combines the advantages of both. Specifically, we use the invertible ResNet to predict the flow field on a sparse grid and apply bilinear interpolation:

$$\mathcal{D}_\theta(\mathbf{x}) = \mathbf{x} + \text{interp}(\mathbf{x}, \mathcal{R}_\theta(\mathbf{P}_c) - \mathbf{P}_c), \quad (10)$$

where $\mathbf{P}_c \in \mathbb{R}^{H \times W \times 2}$ is a sparse grid of fixed control points (pixel locations and $H \times W$ is the resolution of control points instead of images) and \mathcal{R}_θ is an invertible ResNet parameterized by θ .

Unlike existing hybrid neural fields [50] where networks are applied after grid interpolation, our approach uses invertible Residual Networks to predict displacement vectors on a sparse grid where bilinear interpolation is applied to produce a continuous displacement field, shown at the bottom of Fig. 3. The advantage of this architecture is that we only need to compute the expensive forward and backward ResNet mappings for locations at \mathbf{P}_c . This scales with the grid resolution, independent of the number of Gaussians in the scene. The additional operation that needs to be done for each Gaussian is $\text{interp}(\cdot)$, which is affordable and parallelizable.

3.3. Cubemap for Large FOV

In order to apply our method to cameras with larger FOV, we extend the single planar perspective projection to a cubemap projection [35, 61]. Mathematically, single planar projection requires upsampling in the peripheral regions, and the sampling rate increases drastically as the FOV approaches 180° . In contrast, rendering with a cubemap maintains relatively uniform pixel density from the image center to the edges, making it ideal for wide-angle rendering.

Single-planar Projection. Given the parameters estimated from SfM [58], the parametric model is then applied to undistort the raw image into perspective images, as

shown in the blue box in Fig. 2a. These undistorted images are then reconstructed through perspective-based pipelines like NeRF [48] or 3D Gaussian Splatting (3DGS) [37]. However, this process stretches the pixels in the peripheral regions, and the effect becomes more pronounced when undistorting into larger FOV perspectives, as shown in the yellow box. More specifically, the stretching rate of each pixel is defined by the inverse of Eq. (3), which exhibits a trend similar to $\tan(r)$, where r is the FOV angle from the center in the raw image. When the FOV for the undistorted image is 110° (as in the blue example), the upsampling rate from the blue circle to the box is around 1.4. However, when the FOV increases to 170° like the yellow one, this rate rises to 11.4, which inevitably sacrifices a significant amount of high-frequency information for reconstruction.

Moreover, to preserve central details, the resolution of undistorted images needs to be higher, as the pixel density at the center of the raw image should ideally match that of the undistorted perspective. For example, when undistorting a 180° fisheye image in Fig. 2a, the resulting perspective image in the yellow region would have an extremely high resolution, making it computationally infeasible. A common solution is to crop away the periphery, following COLMAP’s approach [58], but this strategy contradicts our intent of using a fisheye camera to capture wide-angle information.

Multi-planar Projections. Inspired by the representation of environment maps using cubemaps in computer graphics [24], we propose representing extreme wide-angle renderings with cubemap projections, each covering 90° FOV and oriented orthogonally to one another, as illustrated in Fig. 2b. By resampling across the cubemap faces, we can render perspective or distorted images with FOVs even larger than 180° . Fast rasterizations are first applied to obtain each face of the cubemap. For each rendered pixel, we look up its corresponding position in the constructed cubemap. Our hybrid distortion field then resamples from the lookup table to achieve the distorted rendering. In practice, it is not necessary to render all faces of the cubemap at once as the choice of number of cubemaps may differ for different FOV camera lenses.

The resampling step only involves a simple coordinate transformation along with our hybrid field distortion. The distance from the shared camera center to each plane is normalized to 1. To render a pixel outside the 90° FOV at $(x, y, -1)$ where $x > 1$ and $|y| < 1$, for instance, the pixel on the right face can be obtained as $(\frac{-1}{x}, \frac{y}{x}, -1)$ in camera coordinates, looking toward the right side. When considering lens distortion, the sampling mapping is distorted according to Eq. (10), altering the lookup on the right face to $(\frac{-1}{x'}, \frac{y'}{x'}, -1)$, where $(x', y') = \mathcal{D}_\theta(x, y)$. By doing so, the entire distortion field can be directly applied to the cubemap

Method	Chairs			Cube			Flowers			Globe			Heart			Rock		
	SSIM	PSNR	LPIPS															
3DGS [37]	0.431	14.06	0.547	0.507	15.21	0.533	0.281	12.91	0.609	0.502	15.09	0.530	0.505	15.19	0.549	0.297	12.70	0.595
Dense-Grid	0.511	15.14	0.525	0.316	13.29	0.581	0.513	15.36	0.517	0.556	16.02	0.489	0.556	16.03	0.489	0.381	13.74	0.527
Sparse-Grid	0.532	15.79	0.442	0.529	16.06	0.513	0.339	14.19	0.560	0.535	16.29	0.502	0.576	16.58	0.475	0.419	15.10	0.482
Adop-GS [55]	0.829	22.59	0.200	0.755	22.12	0.289	0.646	19.96	0.314	0.758	21.35	0.294	0.741	21.37	0.306	0.726	22.48	0.254
Fisheye-GS [46]	0.785	21.68	0.110	0.754	23.29	0.166	0.615	20.23	0.214	0.728	22.11	0.160	0.722	21.37	0.218	0.697	22.38	0.177
Ours	0.832	23.45	0.106	0.786	24.63	0.162	0.693	22.01	0.172	0.790	23.63	0.126	0.775	23.42	0.195	0.787	24.88	0.145

Table 1. **Quantitative Evaluation on the FisheyeNeRF Dataset [34].** We evaluate our method on a challenging real-world benchmark. Our method consistently outperforms existing baselines. More qualitative results are shown in Fig. 4.

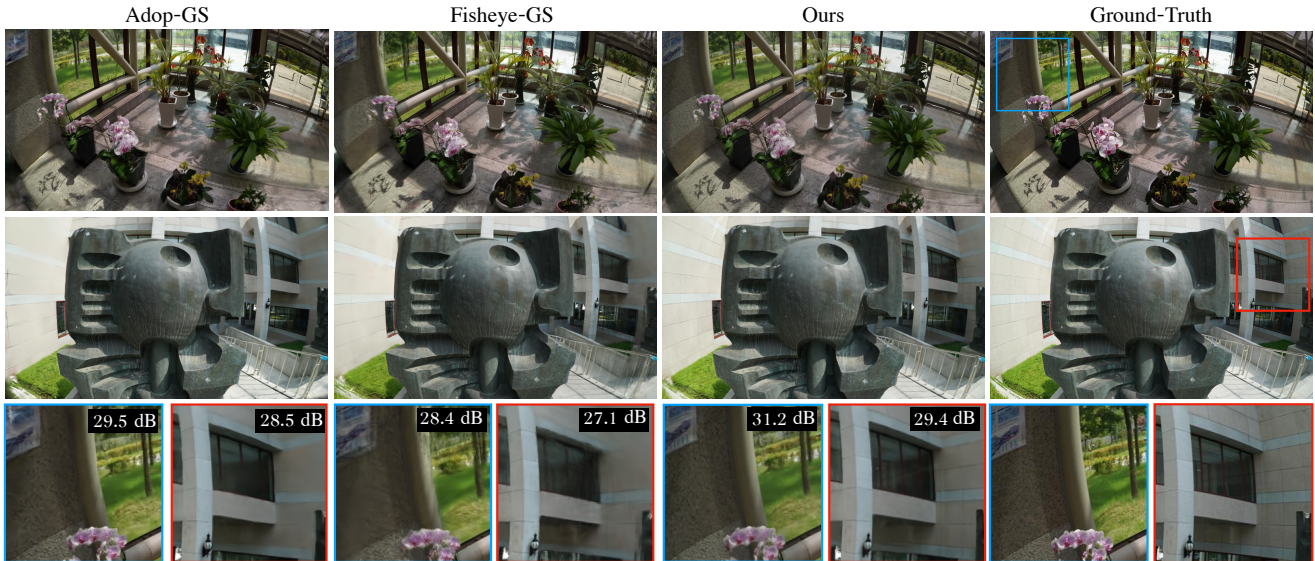


Figure 4. **Qualitative Comparisons with Baselines on the FisheyeNeRF Dataset [34].** The images show comparisons across different scenes using two baselines (e.g., Adop-GS [55] and Fsiheye-GS [46]) and our method. PSNRs are computed for each patch.

for large FOV rendering. The entire resampling process is fully differentiable, making it directly applicable in our hybrid distortion field as a plug-and-play module.

Gaussian Sorting. Vanilla Gaussian Splatting builds an ordered set $\mathcal{N}(G)$ of Gaussians before alpha blending [37]. The Gaussians are sorted based on depth (*i.e.*, the orthogonal projection distance to the image plane). This strategy is valid if a single Gaussian is not projected onto two different faces. However, with the cubemap, Gaussians can span the boundary between two faces, resulting in multiple projections, and the depth ordering is different between the two faces, leading to intensity discontinuities at the boundary. To resolve this, we replace the original sorting by depth with sorting by distance from the camera center to each of the Gaussians. This change ensures that the rasterization order is consistent across all faces of the cubemap, thereby alleviating intensity discontinuities. Due to the affine approximation used in Eq. (5), the 2D covariance of the Gaussians at the cubemap face boundary still has a slight influence on the final render, which we discuss in Sec. 5.

4. Results

In this section, we evaluate our method on both synthetic and real datasets. We will start by describing the dataset we use and the process taken to curate these datasets, followed by comprehensive evaluations.

Synthetic Data. We customized a camera module in the Mitsuba ray tracer [33] to incorporate camera parameters derived from professional DSLR lenses and profiles from the open-source Lensfun database [1]. For scene setup, we rendered three large indoor scenes and four object-centric scenes using 3D assets from [9]. We created a held-out test set where each scene was rendered with paired perspective and fisheye cameras to accurately evaluate the performance of undistortion. To test the efficiency of fisheye captures, we created a training set where the number of fisheye images (*i.e.*, 100) is half that of the narrower FOV perspective images. We applied various levels of lens distortion to the object-centric scenes to evaluate our lens model’s adaptability across diverse camera setups. Additionally, we introduced synthetic distortions, including both radial and tan-

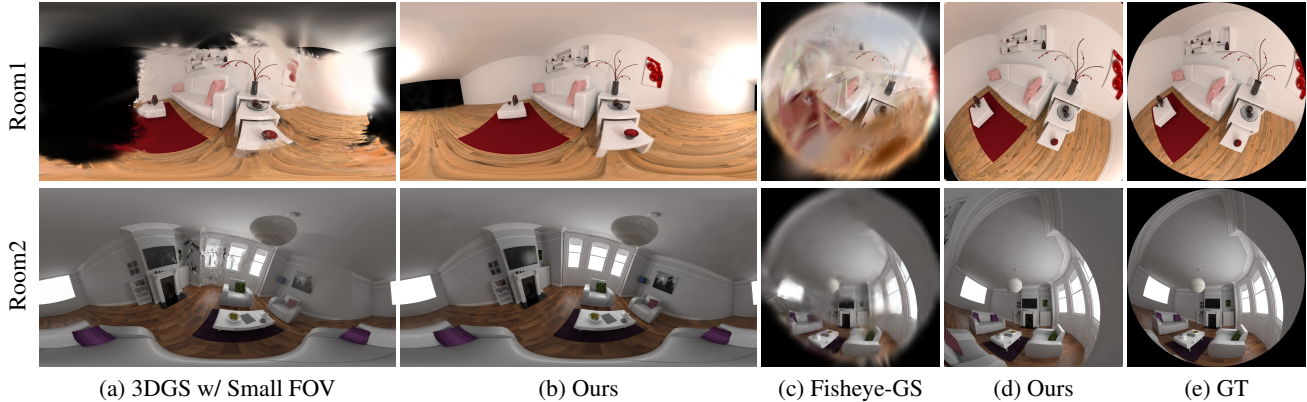


Figure 5. **Qualitative Results on Mitsuba Synthetic Scenes.** To better illustrate reconstruction coverage, we visualize reconstructions using the panorama views of both 3DGS [37] and our method. As explained in Fig. 2, undistorted images compatible with current 3DGS crop large peripheral regions to avoid stretched pixels as the FOV approaches 180° . We also compare our method with Fisheye-GS [46], which fails to reconstruct the peripheral region under extreme distortion.

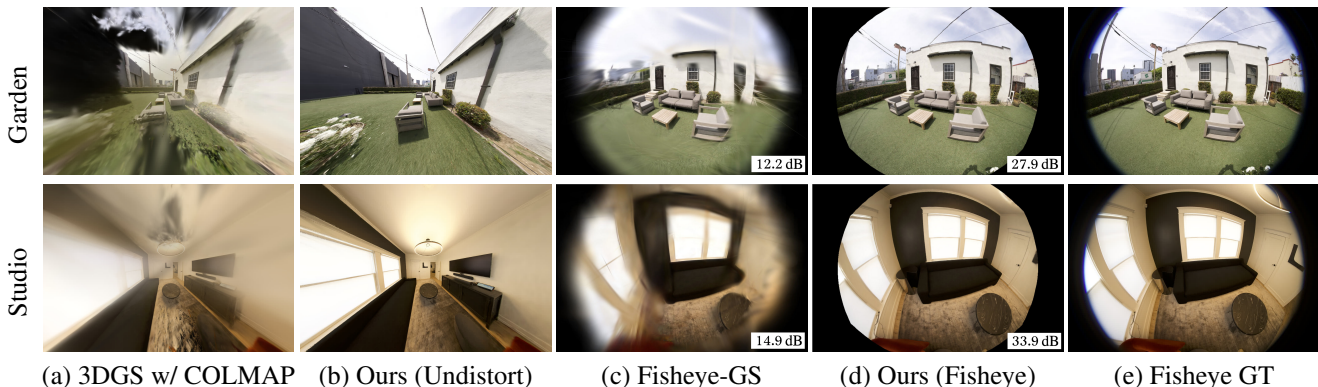


Figure 6. **Qualitative Results on Real-World Captures.** We also evaluate our method on real-world data. 3DGS requires an SfM method like COLMAP [58] but crops the region when the FOV is large. Our method recovers a wider region compared to directly reconstructing from the SfM output. In contrast, Fisheye-GS [46] produces spikes and blurry reconstructions at the edges. We report the average PSNR of hold-out cameras for both Fisheye-GS [46] and our method.

genial components, to images from the LLFF dataset [47]. Further details are provided in the supplementary material.

Real-World Data. We captured several real-world datasets using different uncalibrated cameras to test our method, consisting of casual walk-around video footage with a camera that has a field of view of approximately 150° . Additionally, we evaluated our method on the existing benchmark FisheyeNeRF dataset [34], which consists of highly distorted images captured with ultra-wide-angle fisheye lenses featuring a field of view of around 120° . The dataset includes a variety of indoor and outdoor scenes with complex lighting and geometric details.

4.1. Comparisons with Traditional Lens Models

We evaluate the effectiveness of our hybrid distortion field (Eq. (10)) in modeling substantial fisheye distortions. We

Method	Mitsuba Kitchen			Mitsuba Room1			Mitsuba Room2		
	SSIM	PSNR	LPIPS	SSIM	PSNR	LPIPS	SSIM	PSNR	LPIPS
3DGS [37]	0.470	11.09	0.435	0.595	15.27	0.406	0.897	30.88	0.155
Ours	0.794	27.56	0.272	0.686	26.27	0.314	0.895	33.21	0.172
Fisheye-GS [46]	0.601	14.30	0.485	0.549	15.54	0.548	0.739	17.97	0.355
Ours	0.886	30.72	0.146	0.842	28.46	0.180	0.929	31.16	0.095

Table 2. **Evaluation on Mitsuba Synthetic Scenes.** We compare our method with vanilla 3DGS [37] and Fisheye-GS [46] on a set of held-out captures. Since vanilla 3DGS does not support fisheye rendering, we render several perspective images at the same locations and look-at directions for comparison. We directly compare the fisheye rendering results with both Fisheye-GS and our method. Further details are provided in Sec. 4.1.

use the FisheyeNeRF dataset [34], which consists of full-frame fisheye captures from two indoor and four outdoor scenes. Instead of undistorting images during preprocess-

Type	Method	PSNR	SSIM	LPIPS
Mitsuba Indoor	Vanilla-GS [37]	19.08	0.654	0.332
	Ours (Single Planar)	24.10	0.676	0.312
	Ours (Cubemap)	29.01	0.792	0.253
Mitsuba Objects	Vanilla-GS [37]	25.37	0.923	0.121
	Ours	28.00	0.932	0.093

Table 3. **Evaluation on Mitsuba Synthetic Scenes.** We ablate our cubemap method with a single planar projection using a fixed hybrid distortion field. Single perspective projection utilizes the entire region compared to our cubemap projections, which results in degraded quality. We also compare our method with 3DGS [37] in object-centric scenes with slight radial distortion, where our method still produces better reconstructions.

ing, we directly optimize Gaussians from uncalibrated fisheye photos, simultaneously accounting for camera distortion while optimizing camera parameters and 3D scenes together. We compare our method against four baselines: 1) Vanilla Gaussian Splatting (3DGS); 2) a discrete grid-based method similar to Jeong et al. [34] in both dense (Grid-Dense) and sparse (Grid-Sparse) versions; 3) Fisheye-GS [46], which modifies the 3DGS projection model to a specific type of fisheye parametric camera model; and 4) optimization of the omnidirectional camera model from ADOP [55], which we have re-implemented on GS.

Our method consistently outperforms the baselines in all image metrics, as shown in Tabs. 1 and 2. The baseline methods struggle at the four corners of the images, which can potentially be attributed to using too few parameters to model a complex fisheye camera and bad initializations from SfM, as illustrated in Fig. 4, Fig. 5 (c) and (d), and Fig. 6 (c) and (d). Our method can effectively model lens distortion, resulting in improved reconstruction quality.

4.2. Large FOV Reconstruction.

To verify that large FOV cameras provide better reconstruction coverage than narrower FOV perspective cameras, we evaluate our method on both synthetic Mitsuba scenes and real-world captured scenes.

Our method, directly reconstructed from uncalibrated fisheye images, delivers superior reconstruction quality despite using only half the number of images required by narrower FOV cameras, as the fisheye images capture a larger area in each shot. Quantitatively, we report reconstruction evaluations on the hold-out camera set, as shown in the first two rows of Tab. 2. Reconstruction directly from fisheye captures using our pipeline significantly outperforms the perspective-based reconstruction supported by vanilla 3DGS [37]. As visualized in Fig. 5a and b, our method achieves better coverage in Room1, where all cameras are oriented toward the sofa. Additionally, our method achieves comparable reconstruction with fewer artifacts in a walk-

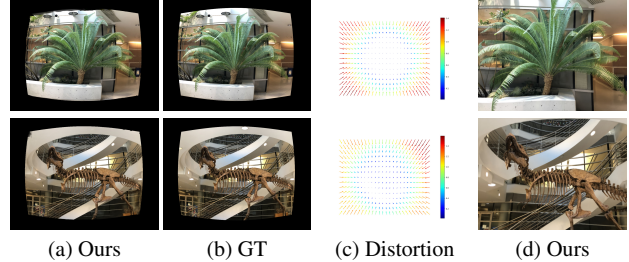


Figure 7. **Qualitative Results of Radial and Tangential Distortion.** We apply synthetic distortion to real-world images and (a) show the distorted rendering, comparing with the reference images in (b). After training, we can use the distortion field in (c) to undistort the image to a perspective view. Notably, we apply a combination of radial and tangential distortion to Trex.

around setting like Room2, even with fewer images.

We further evaluate our method on real-world fisheye captures with over 150° FOV. As a baseline, we apply COLMAP to undistort images from our dataset. We then apply vanilla 3DGS using the undistorted images and our method directly on the raw images, with camera extrinsics and intrinsics estimated by COLMAP. The results are shown in Fig. 6. We find that COLMAP tends to excessively crop the peripheries far from the center of the image, resulting in a significant loss of information (first column). Our approach avoids laborious pre-calibration while retaining details of the original captures, including those in highly distorted areas where information is typically lost during pre-undistortion processes. By optimizing the hybrid distortion field with a multi-planar projection, we are able to utilize the full field of view of fisheye captures, as shown in Fig. 6 (a) and (b).

4.3. Adaptability to Different Lens Distortions.

To verify that our method can model various types of lens distortion, we create synthetic distortions to the images in the LLFF dataset [47]. This simulation mimics various real-world distortions, including radial and tangential distortions, using camera parameters derived from professional DSLR lenses profiled in the open-source Lensfun database. By applying these parameters, we generate the combination of different distortion as shown in the Trex scene. Fig. 7 shows that our method can accurately model various types of camera distortion without the need for manual calibration or access to the physical camera.

4.4. Optimization of Camera Parameters.

Our pipeline also supports camera parameters, including intrinsic and extrinsic optimization, during the reconstruction. The optimization is implemented within native CUDA kernel, making it efficient. Since the main focus is to handle distortion, we leave more experiments and verification of

this capability in the supplementary material.

4.5. Ablation

In this section we validate the necessity of using cubemap resampling for enabling wide FoV reconstruction. We compare the result obtained by our hybrid distortion field using single planar project and using cubemap resampling. We evaluate these two configurations on three wide-angle indoor scenes (*i.e.* Mitsuba Indoor). As presented in Tab. 3, cubemap projections yield significant improvements for 180° fisheyes. Note that both versions of our method outperform the baseline, showing the advantage of using the hybrid distortion field. Additional visualizations are provided in the supplementary.

5. Discussion

This paper presents a method for optimizing Gaussian splat representations while self-calibrating camera parameters and lens distortion. Our approach enables the use of large field-of-view captures to achieve efficient and high-quality reconstruction without cumbersome pre-calibration.

Limitations and Future directions. In this work, we do not address the phenomenon of entrance pupil shift present in most fisheye lenses: rays in the center of the field of view converge at an entrance pupil deeper in the lens than rays at the periphery, which differs from the type of lens distortion we are modeling. In contrast, entrance pupil shift, though insignificant when the scene is distant, can cause splat misalignments for near-field scenes, as the shift can easily be on the order of half a centimeter for full-frame lenses. Additionally, we did not model vignetting (radial brightness falloff) or chromatic aberration. Extending our methods to comprehensively model these effects is a promising direction for future work. Also, since 2D covariances depend on the look-at directions of the cubemap faces onto which the 3D Gaussians are projected, Gaussians located at the boundaries of adjacent cubemap faces will have different 2D covariances, resulting in slight intensity discontinuities. We observe that simply changing the previous depth sorting strategy to distance sorting can largely mitigate these discontinuities. A potentially more elegant solution for future work could be to project the covariances orthogonally to the viewing ray rather than onto the cubemap face.

Societal Impact. This research can benefit industries that depend on 3D reconstruction, such as film production and virtual reality. However, a potential downside is the environmental impact associated with the increased computational resources required for model optimization.

6. Acknowledgement

This work was supported in part by the National Science Foundation under grant 2212084 and the Vannevar Bush Faculty Fellowship. We want to express gratitude to Xichen Pan, Xiangzhi Tong, Julien Philip, Li Ma, Hansheng Chen, Jan Ackermann, and Eric Chen for their discussion and suggestions on this paper.

References

- [1] Lensfun. <https://lensfun.github.io/>. 6, 12
- [2] Miguel Alemán-Flores, Luis Alvarez, Luis Gomez, and Daniel Santana-Cedr s. Automatic lens distortion correction using one-parameter division models. *Image Processing On Line*, 2014. 3
- [3] Lynton Ardizzone, Till Bungert, Felix Draxler, Ullrich K the, Jakob Kruse, Robert Schmier, and Peter Sorrenson. Framework for Easily Invertible Architectures (FrEIA), 2018-2022. 19
- [4] Jiayang Bai, Letian Huang, Jie Guo, Wen Gong, Yuanqi Li, and Yanwen Guo. 360-gs: Layout-guided panoramic gaussian splatting for indoor roaming. *arXiv preprint arXiv:2402.00763*, 2024. 3
- [5] Allison H Baker, Alexander Pinard, and Dorit M Hammerling. Dssim: a structural similarity index for floating-point data. *arXiv preprint arXiv:2202.02616*, 2022. 4
- [6] Jo o Pedro Barreto and Helder Araujo. Geometric properties of central catadioptric line images and their application in calibration. *IEEE TPAMI*, 2005. 3
- [7] Jonathan T Barron, Ben Mildenhall, Dor Verbin, Pratul P Srinivasan, and Peter Hedman. Zip-nerf: Anti-aliased grid-based neural radiance fields. In *ICCV*, 2023. 13
- [8] Jens Behrmann, Will Grathwohl, Ricky TQ Chen, David Duenaud, and J rn-Henrik Jacobsen. Invertible residual networks. In *ICML*, 2019. 2, 4
- [9] Benedikt Bitterli. Rendering resources, 2016. <https://benedikt-bitterli.me/resources/>. 6, 12
- [10] G. Bradski. The OpenCV Library. *Dr. Dobb's Journal of Software Tools*, 2000. 2
- [11] Duane Brown. Decentering distortion of lenses. *Photogrammetric engineering*, 1996. 3
- [12] Martin Bujnak, Zuzana Kukelova, and Tomas Pajdla. New efficient solution to the absolute pose problem for camera with unknown focal length and radial distortion. In *ACCV*, 2010. 3
- [13] Federico Camposeco, Torsten Sattler, and Marc Pollefeys. Non-parametric structure-based calibration of radially symmetric cameras. In *ICCV*, 2015. 3
- [14] Robert Carroll, Maneesh Agrawala, and Aseem Agarwala. Optimizing content-preserving projections for wide-angle images. *ACM TOG*, 2009. 3
- [15] Manmohan Chandraker, Sameer Agarwal, Fredrik Kahl, David Nist r, and David Kriegman. Autocalibration via rank-constrained estimation of the absolute quadric. In *CVPR*, 2007. 2

- [16] Manmohan Chandraker, Sameer Agarwal, David Kriegman, and Serge Belongie. Globally optimal algorithms for stratified autocalibration. *IJCV*, 2010. 2
- [17] Alexander Eugen Conrady. Decentred lens-systems. *Monthly notices of the royal astronomical society*, 1919. 3
- [18] Varuna De Silva, Jamie Roche, and Ahmet Konoz. Robust fusion of lidar and wide-angle camera data for autonomous mobile robots. *Sensors*, 2018. 1
- [19] Frederic Devernay and Olivier Faugeras. Straight lines have to be straight. *Machine vision and applications*, 2001. 3
- [20] C Brown Duane. Close-range camera calibration. *Photogramm. Eng*, 1971. 3
- [21] Jakob Engel, Vladyslav Usenko, and Daniel Cremers. A photometrically calibrated benchmark for monocular visual odometry. *arXiv preprint arXiv:1607.02555*, 2016. 3
- [22] Jiading Fang, Igor Vasiljevic, Vitor Guizilini, Rares Ambrus, Greg Shakhnarovich, Adrien Gaidon, and Matthew R Walter. Self-supervised camera self-calibration from video. In *ICRA*, 2022. 3
- [23] John G Fryer and Duane C Brown. Lens distortion for close-range photogrammetry. *Photogrammetric engineering and remote sensing*, 1986. 3
- [24] Ned Greene. Environment mapping and other applications of world projections. *IEEE computer graphics and Applications*, 1986. 5
- [25] Michael D Grossberg and Shree K Nayar. A general imaging model and a method for finding its parameters. In *ICCV*, 2001. 3
- [26] Michael D Grossberg and Shree K Nayar. The raxel imaging model and ray-based calibration. *IJCV*, 2005. 3
- [27] Kai Gu, Thomas Maugey, Sebastian Knorr, and Christine Guillemot. Omni-nerf: neural radiance field from 360 image captures. In *ICME*, 2022. 3
- [28] Hyowon Ha, Sunghoon Im, Jaesik Park, Hae-Gon Jeon, and In So Kweon. High-quality depth from uncalibrated small motion clip. In *CVPR*, 2016. 3
- [29] Richard Hartley and Sing Bing Kang. Parameter-free radial distortion correction with center of distortion estimation. *IEEE TPAMI*, 2007. 3
- [30] Richard Hartley and Andrew Zisserman. *Multiple view geometry in computer vision*. Cambridge university press, 2003. 3
- [31] Huajian Huang, Yingshu Chen, Tianjian Zhang, and Sai-Kit Yeung. 360roam: Real-time indoor roaming using geometry-aware 360 radiance fields. *SIGGRAPH Asia*, 2022. 3
- [32] Itseez. Open source computer vision library. <https://github.com/itseez/opencv>, 2015. 3
- [33] Wenzel Jakob, Sébastien Speierer, Nicolas Roussel, Merlin Nimier-David, Delio Vicini, Tizian Zeltner, Baptiste Nicolet, Miguel Crespo, Vincent Leroy, and Ziyi Zhang. Mitsuba renderer, 2010. 6, 12
- [34] Yoonwoo Jeong, Seokjun Ahn, Christopher Choy, Anima Anandkumar, Minsu Cho, and Jaesik Park. Self-calibrating neural radiance fields. In *ICCV*, 2021. 2, 3, 6, 7, 8, 12, 13, 17, 18, 19
- [35] Hao Jiang, Gangyi Jiang, Mei Yu, Yun Zhang, You Yang, Zongju Peng, Fen Chen, and Qingbo Zhang. Cubemap-based perception-driven blind quality assessment for 360-degree images. *IEEE TIP*, 2021. 5
- [36] Juho Kannala and Sami S Brandt. A generic camera model and calibration method for conventional, wide-angle, and fish-eye lenses. *IEEE TPAMI*, 2006. 3
- [37] Bernhard Kerbl, Georgios Kopanas, Thomas Leimkühler, and George Drettakis. 3d gaussian splatting for real-time radiance field rendering. *ACM TOG*, 2023. 1, 3, 4, 5, 6, 7, 8, 12, 13, 14, 17, 19
- [38] Shakiba Kheradmand, Daniel Rebain, Gopal Sharma, Weiwei Sun, Jeff Tseng, Hossam Isack, Abhishek Kar, Andrea Tagliasacchi, and Kwang Moo Yi. 3d gaussian splatting as markov chain monte carlo. In *NeurIPS*, 2024. 19
- [39] Diederik P Kingma and Jimmy Ba. Adam: A method for stochastic optimization. *ICLR*, 2015. 19
- [40] Gregor Klančar, Matej Kristan, and Rihard Karba. Wide-angle camera distortions and non-uniform illumination in mobile robot tracking. *Robotics and Autonomous Systems*, 2004. 1
- [41] Georgios Kopanas, Julien Philip, Thomas Leimkühler, and George Drettakis. Point-based neural rendering with per-view optimization. In *Computer Graphics Forum*, 2021. 3, 4
- [42] Zuzana Kukelova, Jan Heller, Martin Bujnak, Andrew Fitzgibbon, and Tomas Pajdla. Efficient solution to the epipolar geometry for radially distorted cameras. In *ICCV*, 2015. 3
- [43] Shreyas Kulkarni, Peng Yin, and Sebastian Scherer. 360fusionnerf: Panoramic neural radiance fields with joint guidance. In *IROS*, 2023. 3
- [44] Hongdong Li and Richard Hartley. Plane-based calibration and auto-calibration of a fish-eye camera. In *ACCV*, 2006. 3
- [45] Longwei Li, Huajian Huang, Sai-Kit Yeung, and Hui Cheng. Omnigs: Omnidirectional gaussian splatting for fast radiance field reconstruction using omnidirectional images. *arXiv preprint arXiv:2404.03202*, 2024. 3
- [46] Zimu Liao, Siyan Chen, Rong Fu, Yi Wang, Zhongling Su, Hao Luo, Linning Xu, Bo Dai, Hengjie Li, Zhilin Pei, et al. Fisheye-gs: Lightweight and extensible gaussian splatting module for fisheye cameras. In *ECCV Workshop*, 2024. 1, 2, 3, 6, 7, 8, 12, 13, 14
- [47] Ben Mildenhall, Pratul P Srinivasan, Rodrigo Ortiz-Cayon, Nima Khademi Kalantari, Ravi Ramamoorthi, Ren Ng, and Abhishek Kar. Local light field fusion: Practical view synthesis with prescriptive sampling guidelines. *ACM TOG*, 2019. 7, 8
- [48] Ben Mildenhall, Pratul P Srinivasan, Matthew Tancik, Jonathan T Barron, Ravi Ramamoorthi, and Ren Ng. Nerf: Representing scenes as neural radiance fields for view synthesis. In *ECCV*, 2020. 1, 5, 13
- [49] Nicolas Moenne-Loccoz, Ashkan Mirzaei, Or Perel, Riccardo de Lutio, Janick Martinez Esturo, Gavriel State, Sanja Fidler, Nicholas Sharp, and Zan Gojcic. 3d gaussian ray tracing: Fast tracing of particle scenes. *SIGGRAPH ASIA*, 2024. 2, 3
- [50] Thomas Müller, Alex Evans, Christoph Schied, and Alexander Keller. Instant neural graphics primitives with a multiresolution hash encoding. *ACM TOG*, 2022. 5

- [51] Linfei Pan, Marc Pollefeys, and Viktor Larsson. Camera pose estimation using implicit distortion models. In *CVPR*, 2022. [3](#)
- [52] Keunhong Park, Philipp Henzler, Ben Mildenhall, Jonathan T Barron, and Ricardo Martin-Brualla. Camp: Camera preconditioning for neural radiance fields. *ACM TOG*, 2023. [3](#), [13](#)
- [53] Marc Pollefeys and Luc Van Gool. Stratified self-calibration with the modulus constraint. *TPAMI*, 1999. [2](#)
- [54] Marc Pollefeys, Reinhard Koch, and Luc Van Gool. Self-calibration and metric reconstruction inspite of varying and unknown intrinsic camera parameters. *IJCV*, 1999. [3](#)
- [55] Darius Rückert, Linus Franke, and Marc Stamminger. Adop: Approximate differentiable one-pixel point rendering. *ACM TOG*, 2022. [3](#), [6](#), [8](#)
- [56] Davide Scaramuzza, Agostino Martinelli, and Roland Siegwart. A flexible technique for accurate omnidirectional camera calibration and structure from motion. In *ICVS*, 2006. [3](#)
- [57] Davide Scaramuzza, Agostino Martinelli, and Roland Siegwart. A toolbox for easily calibrating omnidirectional cameras. In *IROS*, 2006. [3](#)
- [58] Johannes Lutz Schönberger and Jan-Michael Frahm. Structure-from-motion revisited. In *CVPR*, 2016. [1](#), [2](#), [3](#), [5](#), [7](#), [12](#), [14](#), [15](#), [16](#), [17](#), [19](#)
- [59] Johannes Lutz Schönberger, Enliang Zheng, Marc Pollefeys, and Jan-Michael Frahm. Pixelwise view selection for unstructured multi-view stereo. In *ECCV*, 2016. [1](#)
- [60] Ellen Schwalbe. Geometric modelling and calibration of fisheye lens camera systems. In *ISPRS*, 2005. [3](#)
- [61] Liang Wan, Tien-Tsin Wong, and Chi-Sing Leung. Isocube: Exploiting the cubemap hardware. *TVCG*, 2007. [5](#)
- [62] Wenqi Xian, Aljaž Božič, Noah Snavely, and Christoph Lassner. Neural lens modeling. In *CVPR*, 2023. [2](#), [3](#), [4](#)
- [63] Linning Xu, Vasu Agrawal, William Laney, Tony Garcia, Aayush Bansal, Changil Kim, Samuel Rota Bulò, Lorenzo Porzi, Peter Kotschieder, Aljaž Božič, et al. Vr-nerf: High-fidelity virtualized walkable spaces. In *SIGGRAPH Asia*, 2023. [3](#)
- [64] Vickie Ye, Ruilong Li, Justin Kerr, Matias Turkulainen, Brent Yi, Zhuoyang Pan, Otto Seiskari, Jianbo Ye, Jeffrey Hu, Matthew Tancik, and Angjoo Kanazawa. gsplat: An open-source library for Gaussian splatting. *arXiv preprint arXiv:2409.06765*, 2024. [19](#)
- [65] Wang Yifan, Felice Serena, Shihao Wu, Cengiz Öztireli, and Olga Sorkine-Hornung. Differentiable surface splatting for point-based geometry processing. *ACM TOG*, 2019. [3](#), [4](#)
- [66] Zehao Yu, Anpei Chen, Binbin Huang, Torsten Sattler, and Andreas Geiger. Mip-splatting: Alias-free 3d gaussian splatting. In *CVPR*, 2024. [19](#)
- [67] Cyril Zeller and Olivier Faugeras. *Camera self-calibration from video sequences: the Kruppa equations revisited*. PhD thesis, INRIA, 1996. [2](#)
- [68] Zhengyou Zhang. Flexible camera calibration by viewing a plane from unknown orientations. In *ICCV*, 1999. [3](#)
- [69] Matthias Zwicker, Hanspeter Pfister, Jeroen Van Baar, and Markus Gross. Ewa volume splatting. In *Visualization*, 2001. [4](#)

Self-Calibrating Gaussian Splatting for Large Field of View Reconstruction

Supplementary Material

1. Supplementary Video

We provide a video to better compare our methods with baselines. Our video is organized into three different parts.

The first part is a comparison between our method and baselines on the FisheyeNeRF Dataset [34] across three scenes. Vanilla 3DGS [37] fails completely to reconstruct the scenes because lens distortion is not accounted for. Fisheye-GS [46] adopts a parametric model, but the peripheral regions produce blurry results, as highlighted by the red box in the corners. In contrast, our method achieves clean and sharp reconstructions.

The second part of the video shows reconstruction results using our method of walk-around captures. These include both synthetic and real-world scenes. Our approach achieves sharp and clean renderings once completing the reconstruction.

The last part of the video compares visualization of our method and a conventional reconstruction pipeline that either uses narrow FOV perspective images or undistorted images from COLMAP [58] as input. Our method can successfully reconstruct larger regions, particularly for scenes captured with large 180° cameras. Besides, we render videos in fisheye views for each scene.

2. Synthetic Data Creation

To carefully control the experimental settings, we customized a camera module in the Mitsuba ray tracer [33] using camera parameters derived from DSLR lenses, as profiled in the open-source Lensfun [1]. We also utilize 3D assets, including geometry, materials, and lighting from [9] to produce renderings. Our synthetic dataset contains three large indoor scenes and four object-centric scenes. All indoor scenes follow a Sigma 180° circular fisheye camera. Two of the object scenes are rendered with a 120° fisheye lens, and the others are rendered with classic radial distortion.

To capture detailed perspectives of the scene, cameras are placed close to the objects at varying distances. For Room2, since objects were uniformly distributed in the space, we placed a set of camera centers along a Hilbert curve, then look out from each fix camera center to cover the surroundings. The number of images captured at each point is reduced by half for 180° images compared to those with 100° FOV.

In order to verify the accuracy of self-calibration, we also generate a set of hold-out cameras that share the same distribution as the training set. For each validation camera, we render paired perspective and 180° fisheye images. Unlike

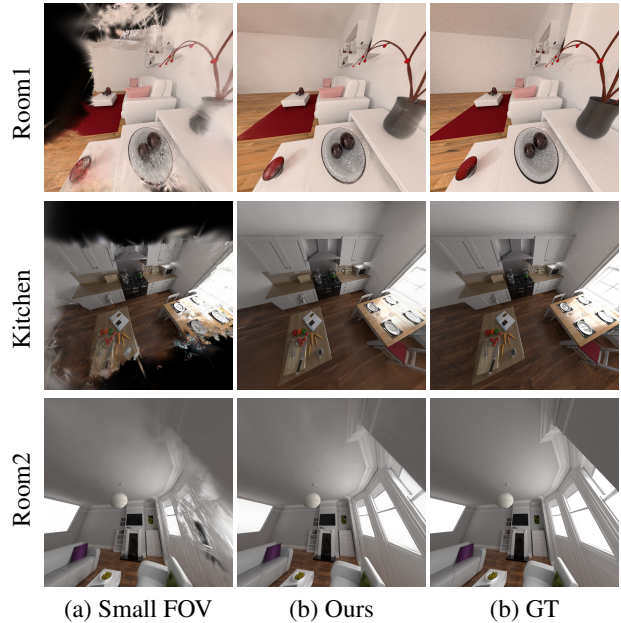


Figure 8. **Evaluation of Perspective Rendering.** After reconstruction, our method can render perspective views with arbitrary FOV. We compare the perspective renderings produced by our method with those rendered from small-FOV reconstructions using 3DGS [37].

real-world datasets such as Garden and Studio, our synthetic dataset allows comparison with Ground-Truth perspective views. As shown in Fig. 8, we render an additional 20° for the hold-out cameras to show the difference in coverage between our method and conventional capture approach.

3. Extra Comparisons with Baseline

In addition to Fig. 6 in the main paper, we also provide a quantitative evaluation of our method compared with the baseline Fisheye-GS [46]. The performance degradation observed in the baseline method is primarily due to the limitations of the parametric model used during reconstruction, which struggles with the edge of large FOVs. As a result, there is no geometric consistency in the peripheral regions to produce uniform gradients for optimizing the Gaussians. When rendering novel views, these Gaussians appear as large floaters that occlude the camera view. We further visualize this phenomenon in the failure case video reconstructed by Fisheye-GS [46]. The center area was revealed as we gradually decreased the scale of the Gaussians. Please refer to our supplementary videos under “section3_video” directory for the comparison with the parametric distortion

Method	Garden			Studio		
	SSIM	PSNR	LPIPS	SSIM	PSNR	LPIPS
Fisheye-GS [46]	0.530	14.94	0.542	0.536	12.24	0.549
Ours	0.882	27.85	0.144	0.965	33.86	0.044

Table 4. **Evaluation on Real-World Wide-Angle Captures.** We evaluate Fisheye-GS [46] and our method on two real-world scenes captured with large FOV fisheye cameras. Our method outperforms the baseline by a significant margin.



(a) Low Resolution (b) High Resolution

Figure 9. **Resolution of Control Grid.** When the resolution of the control grid is decreased, the central region retains decent quality due to minimal distortion. However, as highlighted by the red and blue boxes in the corners of the image, a sparse control grid for the hybrid field results in noticeably distorted renderings.

model.

4. Optimization of Camera Parameters

In this section, our method can accurately recover the camera parameters of a perspective pinhole camera model. We use the NeRF-Synthetic dataset [48], which includes known ground truth camera poses. The dataset contains 100 viewpoints for training and 200 additional viewpoints for computing test error metrics. We first add noise to perturb the rotation angles of camera extrinsics, the positions of the camera centers, and the focal lengths. These noisy cameras are used to train both the baselines and our methods. We compare our methods with CamP [52] implemented on ZipNeRF [7], a state-of-the-art method for joint optimization of 3D scene and camera extrinsics and intrinsics. In addition to CamP, we also report the performance of vanilla Gaussian Splatting without pose optimization.

The models are evaluated on two criteria, following the protocol in CamP [52]. First, we measure the accuracy of the estimated camera pose in the training views after accounting for a global rigid transformation. Second, we measure the quality of rendered images at the held-out camera poses after a test-time optimization to adjust the held-out pose for a potential global offset. Tab. 5 shows that our method can outperform both vanilla 3DGS and CamP in both image and camera metrics by a large margin.

Methods	Image Metrics			Camera Metrics	
	PSNR	SSIM	LPIPS	Position	Orientation
3DGS	16.54	0.733	0.273	0.2911	5.015
CamP	19.07	0.840	0.289	0.1879	5.619
Ours	32.84	0.964	0.034	0.0082	0.919

Table 5. Comparison with CamP [52] and 3DGS [37] in the NeRF-Synthetic dataset. We report average camera orientation errors in degrees, and position error in world units.

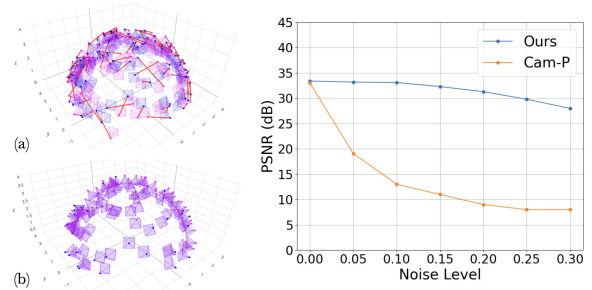


Figure 10. Visual comparison of (a) the initial perturbed ($s = 0.15$) and GT poses and (b) optimized camera poses in the Lego scene. The chart demonstrates the different level of perturbations and the effectiveness of our optimization. Our method successfully recovers accurate camera frames.

We further test our model by perturbing the camera poses with different levels of noise. Specifically, we add Gaussian noise with a standard deviation ranging from 0 to 0.3 to the camera poses. Adding larger noise to camera poses is very challenging. Fig. 10 and Fig. 11 show that CamP’s performance significantly drops since it is prone to falling into local minima when the initial camera poses have significant errors, while our method shows much slower degradation in novel-view synthesis performance.

5. Computational Efficiency

Training Time. To verify the hypothesis that our hybrid method allows us to find a better combination of expressivity and speed, we perform an ablation study on the FisheyeNeRF dataset [34]. Specifically, we study the grid resolution for P_c , which determines the number of evaluations needed for the most expensive part of the pipeline – the invertible ResNet. Table 6 reports the PSNR and training time for three different grid resolutions, Fisheye-GS [46], and vanilla 3DGS [37]. We can see that higher resolution P_c leads to better performance but longer training time. Reducing the grid resolution further does not lead to shorter computation time, since other operations, such as the gradient computation for other camera parameters, start to dominate. Fortunately, all hybrid solutions significantly outperform vanilla 3DGS and Fisheye-GS. The lowest resolution we tried introduces only 7 minutes of training time over-

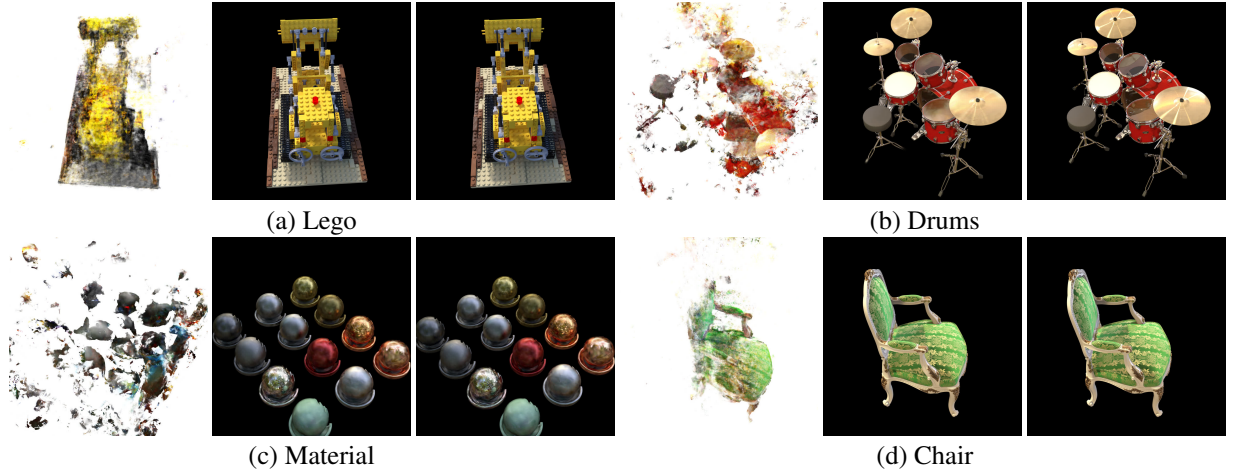


Figure 11. We carry qualitative comparison with CamP at noise level 0.15. Each scene show CamP, our method, and the ground truth, from left to right. Our method is able to produce sharp renderings at this noise level, where CamP fails.

P_c Resolution	PSNR (\uparrow)	Time (mins)
265×149	23.67	55
132×74	22.99	36
66×37	22.44	25
Explicit Grid	14.93	22
Fisheye-GS [46]	21.84	46
3DGS [37]	14.19	18

Table 6. **Ablation Study on Control Grid Resolution.** Parameter study on different control point resolutions, showing that our method has favorable cost/performance trade-off.

head on top of 3DGS, in exchange for a > 8 dB boost in PSNR.

Control Grid Resolution. A higher resolution control grid results in a smoother distortion field representation. To better illustrate the effect of control grid resolution, we visualize two types of resolutions (*i.e.*, 265×149 and 66×37). While there are no significant differences in the central region, the distortion at the edges is better recovered with a higher resolution grid. Since the distortion field becomes smoother, a high-resolution control grid produces more accurate distorted lines, as shown in the red and blue boxes of Fig. 9.

6. Real-world Walk-around Scenes

We use a Canon 5D Mk III DLSR camera with a Canon 8mm-15mm Fisheye lens zoomed out to 8mm with a 180° FOV to capture a complex indoor office scene, where we place models and spheres on a table. Images are taken close

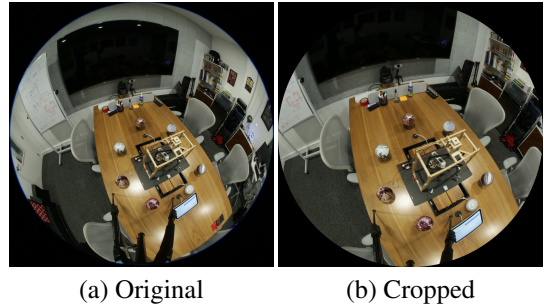
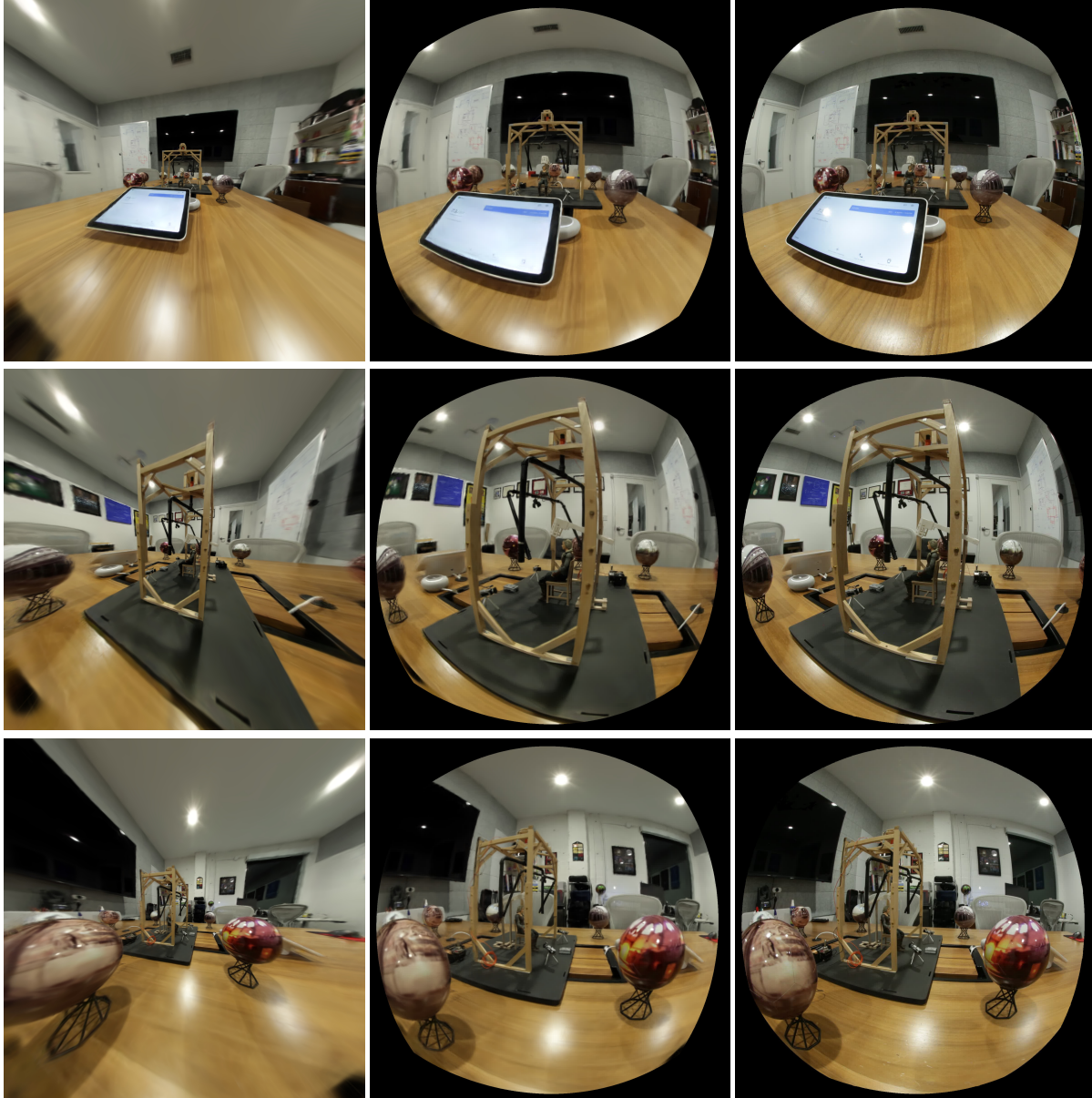


Figure 12. **Preprocessing of Ultra Wide Angle.** Meike camera we used has a FOV of 220° , which means it project scenes on the back of images plane. In this case, our first step of estimating extrinsic will fail in COLMAP [58]

to the table to capture the details of the various models and spheres. We also use Meike 3.5mm f/2.8 Ultra Wide-Angle Circular Fisheye Lens capture the same office. However, in practice, we did not fully utilize the entire 220° field of view, primarily because the ultra-wide angle often includes the tripod at the bottom (handholding is impractical, as the human body would also appear in the lower region). Moreover, when the raw 220° images are fed into COLMAP [58], the SfM pipeline fails because this camera captures scenes from the back, and the projection models predefined in COLMAP [58] do not support back-facing projections. Consequently, we crop the raw images slightly to reduce the FOV to 180° and partially exclude the tripod’s influence like Fig. 12. Qualitative results are shown in Fig. 13. Our method effectively recovers details in the central region while producing accurate lens distortion for background elements, such as painting frames and lines on



(a) Ours (Perspective)

(b) Ours (Fisheye)

(c) GT

Figure 13. **Reconstruction from 180° FOV Fisheye Captures.** Using a Canon fisheye camera, we capture the scene and reconstruct the office with our method. Both perspective and fisheye views are rendered to demonstrate the quality of our reconstruction.

the white wall.

We also mount two fisheye cameras on a rig configured such that the cameras are perpendicular to each other. This camera rig is used to capture a backyard scene by walking clockwise and counterclockwise twice to record videos. The benefit of using this rig is that the relative pose between the two fisheye cameras is fixed, simplifying the SfM [58] pipeline for estimating accurate poses. As shown in Fig. 14, our method converges to an accurate calibration, ensuring that lines on the house’s surface and the ladder leaning on

the tree are straight when rendered in perspective views.

7. Additional Ablation Studies

Ablation of Cubemap As illustrated in Fig. 2 of the main paper, we apply cubemap to deal with the limitation of perspective projection. Even with our hybrid distortion field, we can only take advantage of center part of raw fisheye images as shown in the bottom row of Fig. 15. In contrast, rendering cubemap allows us to expand to larger FOV and

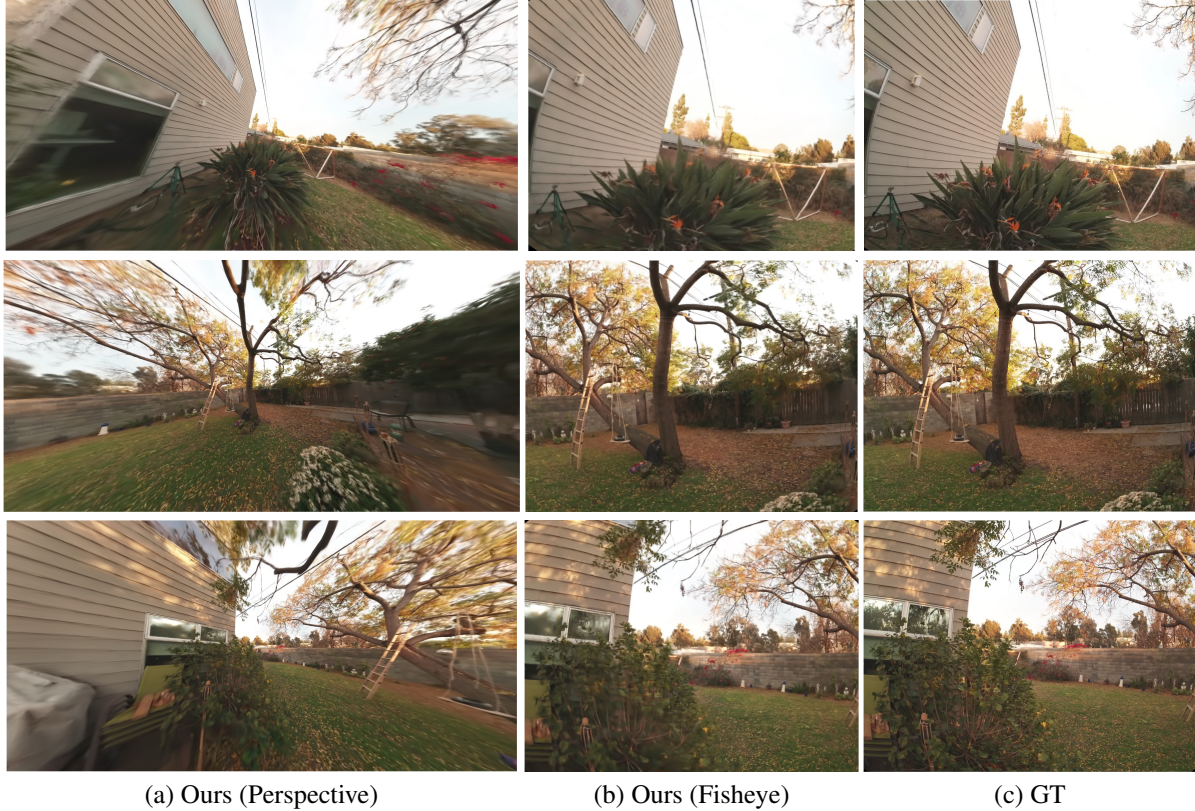


Figure 14. **Large FOV Reconstruction from a Customized Fisheye Rig.** We reconstruct a backyard from images captured using a fisheye rig. Our method achieves accurate geometric corrections, such as straightening the lines on the wall and the edges of the house.

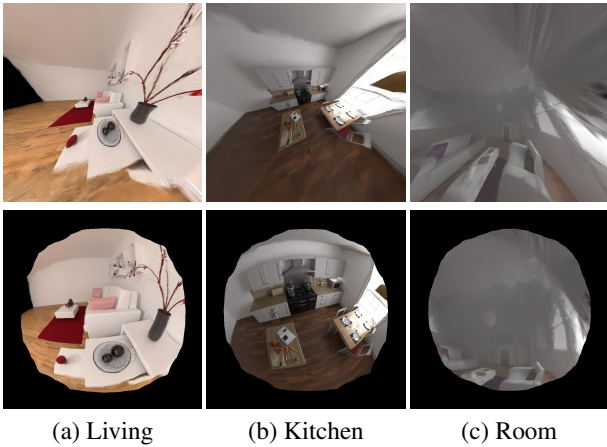


Figure 15. **Single Planar Projection with Hybrid Field.** Our hybrid field can be directly applied to a single plane during rasterization. However, the limitation of single planar projection is that it cannot cover the full FOV of the raw images, leading to partial loss of information in the peripheral regions.

thus compute the photometric loss with reference raw images for optimization like Fig. 5 (d) in the main paper. Be-

cause of the rendering FOV of single planar projection and cubemap, the final reconstruction quality is compromised as shown in Tab. 3 of the main paper.

Besides, the boundary of the final distorted rendering is irregular, largely because the distortion information at the boundary heavily relies on the extra regions that are not covered by single planar projections.

Ablation of Hybrid Field Optimization. In practice, the estimated distortion from the SfM [58] pipeline can be used as an initialization for our hybrid field, which makes training stable and achieves faster convergence. However, these parameters may be inaccurate when solving from highly distorted images. We verify the necessity of optimizing our hybrid field during reconstruction both quantitatively and qualitatively. If we assume the distortion parameters are accurate and expressive enough to model lens distortion, we can freeze the hybrid field after initialization from SfM. While the hybrid field can produce a roughly correct distortion field, it leads to blurry reconstructions, as shown in Fig. 16. This degradation becomes more pronounced in scenes with many straight lines, such as the jalousie windows in chairs scene. The photometric evaluation in Tab. 7

Method	Chairs			Cube			Flowers			Globe			Heart			Rock		
	SSIM	PSNR	LPIPS															
3DGS [37]	0.431	14.06	0.547	0.507	15.21	0.533	0.281	12.91	0.609	0.502	15.09	0.530	0.505	15.19	0.549	0.297	12.70	0.595
COLMAP+GS	0.583	18.28	0.290	0.637	21.64	0.296	0.443	18.09	0.379	0.580	19.63	0.327	0.660	20.87	0.282	0.511	20.24	0.280
Ours	0.832	23.45	0.106	0.786	24.63	0.162	0.693	22.01	0.172	0.790	23.63	0.126	0.775	23.42	0.195	0.787	24.88	0.145

Table 7. **Quantitative Comparison on Invertible ResNet Optimization.** We compare our final optimized hybrid field with a fixed hybrid field reconstruction on FisheyeNeRF [34]. While the distortion estimated from COLMAP [58] significantly improves quality compared to vanilla 3DGS [37], optimizing the invertible ResNet further enhances performance.

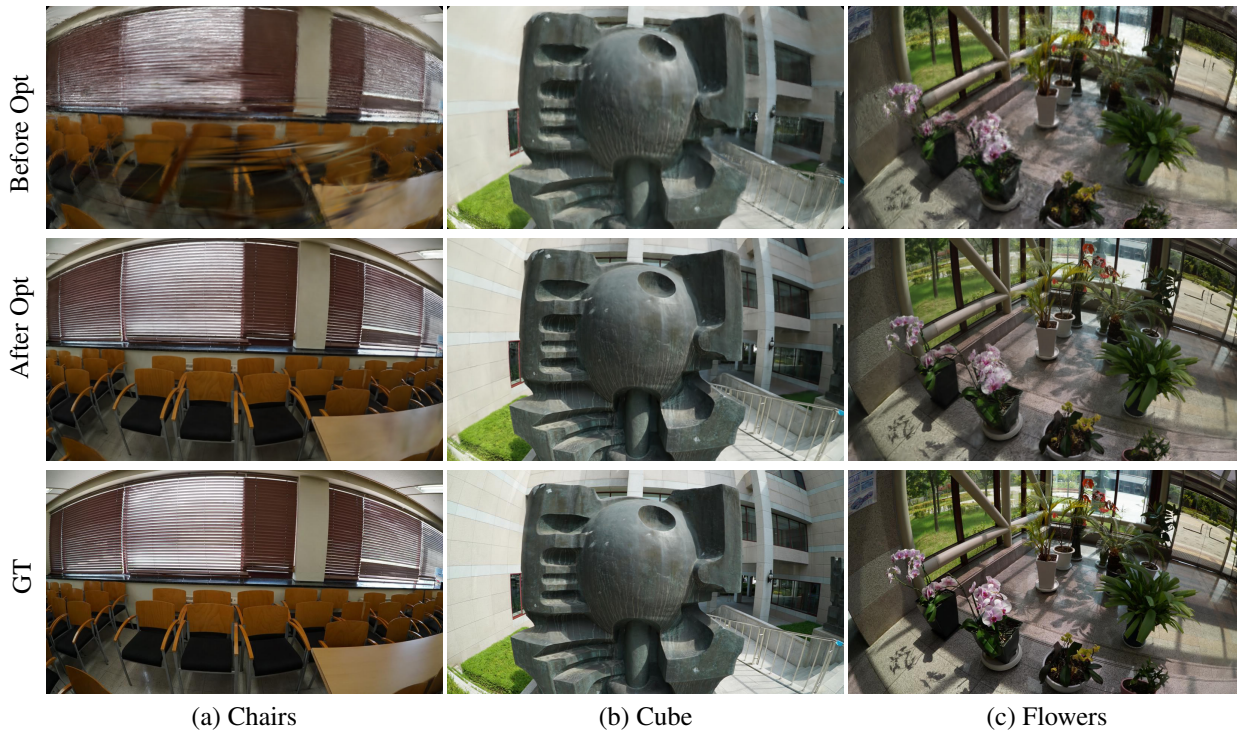


Figure 16. **Qualitative Comparison on Invertible ResNet Optimization.** Here is a comparison demonstrating the differences before and after optimizing our lens model on scenes from FisheyeNeRF dataset.

shows our final hybrid field can outperform estimated distortion parameters by a large margin. Optimizing our hybrid field is crucial for achieving more accurate reconstruction and distortion modeling.

Ablation Effective Regularization of iResNet. Neural networks can model complex non-linear fields, but the key advantage of iResNet is its effective regularization. Light rays passing through the lens are strictly bijective and invertible. iResNet, using fixed-point iteration, enforces this property at minimal cost. We visualize the error map compared to the distortion of the GT lens in synthetic scenes in Fig. 17. We show that iResNet predicts smooth distortion with low error, whereas ResNet produces a highly asymmetric field with large errors. The large error produced by ResNet is largely due to the lack of regularization. The displacement predicted by ResNet can be arbitrary and does

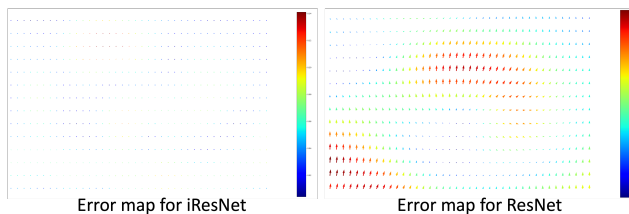


Figure 17. **Distortion Error Map.** We visualize the error map between the predicted distortion and the ground truth distortion from Mitsuba synthetic scenes.

not follow the two properties that real-world light rays hold.

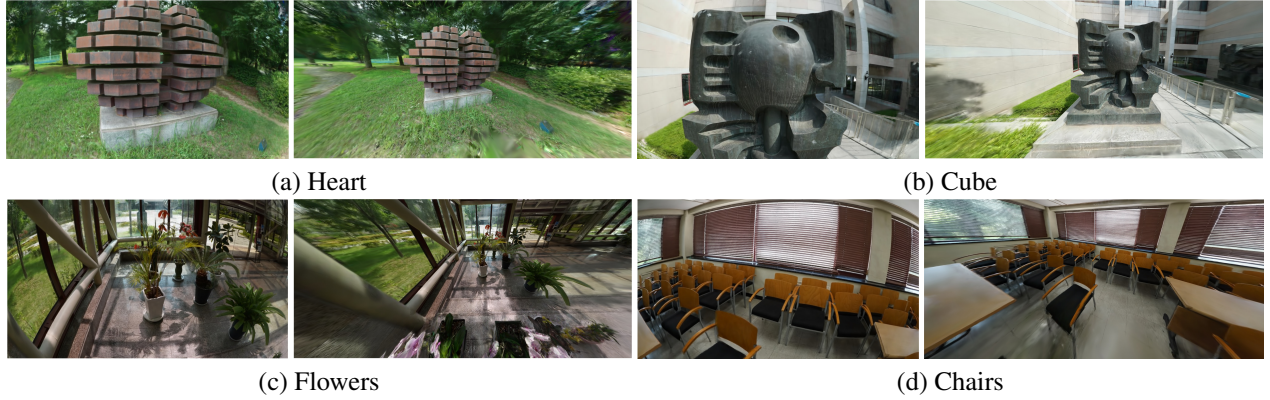


Figure 18. **Fisheye and Perspective Rendering.** After optimization, our method allows rendering in either fisheye or perspective views. Perspective rendering can be achieved by simply removing the hybrid field.

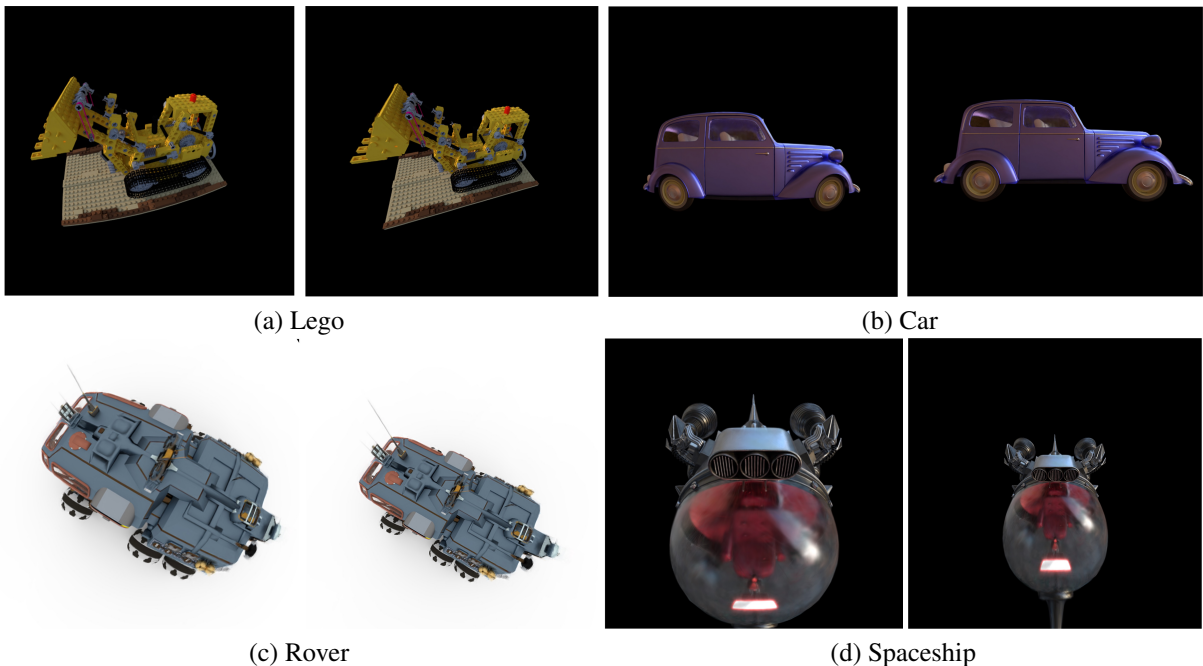


Figure 19. **Radial and Perspective Rendering.** We evaluate our method on a synthetic radial distortion dataset. Our approach successfully recovers slight radial distortion during reconstruction and enables perspective rendering upon completion of training.

8. Additional Results

FisheyeNeRF Scenes [34]. We provide more rendering results in this section. We render both fisheye and perspective view on FisheyeNeRF dataset [34]. In Fig. 18, we render fixed the view direction and camera location of fisheye rendering and extend the FOV of perspective rendering. As for scenes such as cube, chairs, and flowers, we can see the straight lines are nicely recovered during the reconstruction. The lines on the wall back of cube and lines on the windows are good proof that our self-calibration system accurately model lens distortion.

Synthetic Radial Objects. We apply moderate radial distortion to our synthetic dataset and reconstruct several object scenes. After training, we can render undistorted images. The perspective rendering increases the FOV while maintaining the same camera extrinsics. As shown in Fig. 19, distorted edge lines, such as those on the Lego and Car objects, are correctly recovered into straight lines, demonstrating the capability of our hybrid field to model radial distortion effectively.

9. Implementation Details

Our implementation is based on the codebase by Gaussian Splatting [37] and gsplat [64]. The invertible ResNet is constructed using FrEIA [3]. We follow Kerbl et al. [37] to select hyper-parameters for optimizing 3D Gaussians. We also adopt the implementation of MCMC densification [38]. We notice that compared with vanilla densification, MCMC can help to remove floaters by using opacity thresholding to relocate dead Gaussians. While the final quantitative number in the test set remains roughly unchanged, applying the MCMC technique produces fewer visual floaters in novel viewpoints. For high-resolution scene captures, such as Backyard and Office, we also use bilateral grid and anti-aliasing [66] for better quality. As explained in Fig. 16, optimizing our hybrid field is essential for successful self-calibration. We use Adam [39] for the invertible ResNet. The initial learning rate for the invertible ResNet is set at $1e-5$ and decreases to $1e-7$ for FisheyeNeRF [34]. The final learning rate for real-world captures is $1e-8$, including Studio, Garden, Backyard in Figure 14, and more complex real-world captures like Office Fig. 13. The learning rate for Mitsuba indoor synthetic scenes is set to $1e-8$, while objects are $1e-7$. After estimating distortion parameters from COLMAP, we uniformly sample points following the estimated distortion parameters to initialize the invertible ResNet, which typically takes approximately 1 minute to complete. All experiments are conducted on a single NVIDIA GeForce RTX 3090.

10. Failure Cases and Limitations

Real-world outdoor captures often include the sky. Reconstructing the sky poses challenges due to moving clouds and the large uniform region of blue and white without textures. The 3DGS [37] method tends to assign large Gaussians to the sky, resulting in artifacts when rendering novel views. Occasionally, some large Gaussians leak into the scene’s center, appearing as a thin film in front of the camera. Similarly, for indoor scenes, regions with uniform textures, such as colored walls, present challenges. These textureless walls are often represented by Gaussians with large covariant matrix, causing similar rendering artifacts as observed with the sky.

The Gaussian sorting we propose alleviates the intensity discontinuities at the boundaries of cubemap faces caused by the multiple projections of a single Gaussian. However, since the projection of 3D covariance follows Equation 5 in the main paper, identical 3D Gaussians can still result in different 2D covariates on different faces. This issue can be addressed by implementing smoother transitions between projection faces.

As mentioned in Section 6, we rely on COLMAP [58] to obtain the extrinsic parameters of the camera pose. How-

ever, the projection models defined in COLMAP cannot handle the peripheral regions projected from the back of the image plane, leading to complete failure. We circumvent this by manually cropping the raw images into smaller FOVs before inputting them into COLMAP. It would be interesting future direction to improve the reconstruction pipeline to handle this issue automatically.

Finally, we do not account for the entrance pupil shift phenomenon commonly observed in fisheye lenses. This effect is distinct from the lens distortion we are currently modeling. As a result, our method still struggles with such cameras, as shown in Figure 13. While entrance pupil shift is negligible for distant scenes, it can cause splat misalignments in near-field scenes (*e.g.*, the blurry sphere surface in the Office scene shown in the video), as the shift can reach up to half a centimeter for full-frame lenses. It remains an exciting direction to study how to model such lens effects to further improve reconstruction qualities.